Research Square

Preprints are preliminary reports that have not undergone peer review.
They should not be considered conclusive, used to inform clinical practice,
or referenced by the media as validated information.

Spectral overlap and molecular sampling in Raman enhancement at nanoparticle oxide metal interfaces

Patricia M. A. Farias

patricia.mafarias@ufpe.br

Federal University of Pernambuco (UFPE)

Priscila Vilemen

Federal University of Pernambuco (UFPE)

Nathalia B. Lima

Federal University of Pernambuco (UFPE)

Andreas Stingl

Phornano Holding GmbH

Olavo Cardozo

Northeast Centre for Strategic Technologies - CETENE

Research Article

Keywords: Surface-enhanced Raman scattering, Optical reciprocity, Spectral overlap, Spatial correlation, Nanoparticle–metal interfaces, Plasmonic coupling

Posted Date: November 19th, 2026

DOI: https://doi.org/10.21203/rs.3.rs-11519070/v1

License: This work is licensed under a Creative Commons Attribution 4.0 International License.
Read Full License

Additional Declarations: No competing interests reported.

Spectral overlap and molecular sampling in Raman enhancement at nanoparticle oxide metal interfaces

Patrícia M. A. Farias[a]*; Priscila Vilemen[a]; Nathalia B. Lima[a]; Andreas Stingl[b]; Olavo Cardozo[a,c],[c]

a Laboratory for Advanced Materials, Graduate Program on Materials Science, Federal University of Pernambuco (UFPE), Recife, PE 50670-901, Brazil

b Phornano Holding GmbH, Kleinengersdorferstrasse 24, 2100 Korneuburg, Austria

c Northeast Centre for Strategic Technologies (CETENE), Recife, PE 50740-545, Brazil

*Corresponding author. E-mail: patricia.mafarias@ufpe.br. Full postal address: Laboratory for Advanced Materials, Graduate Program on Materials Science, Federal University of Pernambuco (UFPE), Av. Prof. Moraes Rego, 1235, Cidade Universitária, Recife, PE 50670-901, Brazil.

Article type: Original Paper

Acknowledgements

The authors thank the Laboratory for Advanced Materials at the Federal University of Pernambuco (UFPE) and the Northeast Centre for Strategic Technologies (CETENE) for institutional support and computational resources.

This work received no direct project grant. The authors acknowledge the general institutional support of the Austrian Research Promotion Agency (FFG), the Brazilian National Council for Scientific and Technological Development (CNPq), and the Brazilian Federal Agency for Support and Evaluation of Graduate Education (CAPES).

Abstract

Far-field plasmon spectra are often used to select surface-enhanced Raman scattering (SERS) excitation wavelengths, although the molecular response samples two frequencies and spatially registered sites. We formulate a reciprocal response kernel for nanoparticle–oxide–metal interfaces and combine analytical ranking tests with full-wave spectral and geometry sweeps. A prescribed Lorentzian example gives a 5.85-fold two-frequency advantage to a resonance with a lower peak; independent center optimization retains a 5.76-fold advantage. For 60 nm-radius gold spheres above oxide-covered aluminum, a 500–900 nm pump scan gives a sampled mean-kernel maximum at 595 nm, compared with 580 nm for upward particle scattering and 680 nm for a pump-only fourth-power proxy. One-factor sweeps cover oxide thicknesses of 1–5 nm, air spacers of 3–7 nm and interparticle gaps of 10–30 nm, with particle dimensions and molecular sampling held consistently defined. At 633 nm, the largest sampled parameter-dependent response span is 54.41-fold for interparticle gap. Registered fields also quantify the wavelength-dependent error of multiplying separate excitation and emission averages. The results show how spectral overlap and molecular-site weighting jointly determine supported-substrate rankings. They are conditional predictions for prescribed geometries and two equally occupied reporter sites, not experimental validation of a fabricated deposit or a concentration detection limit.

Keywords: Surface-enhanced Raman scattering; Optical reciprocity; Spectral overlap; Spatial correlation; Nanoparticle–metal interfaces; Plasmonic coupling

1 Introduction

Gold nanoparticle deposits on aluminum foil offer an accessible platform for surface-enhanced Raman scattering (SERS), but the active optical object is the deposited nanoparticle–oxide–metal system rather than the precursor suspension [1–3]. The support changes the driving field, particle self-interaction, coupling between neighboring particles and the radiation admitted by the detector. Consequently, a transmission-extinction maximum measured before deposition cannot, by itself, identify the best excitation wavelength or rank the final substrates. The distinction between a far-field resonance and a molecular enhancement is established in plasmonic spectroscopy [4–8]. Near-field and far-field maxima can occur at different frequencies, while the strongest SERS sites occupy only a small part of an illuminated structure [9–11]. A Stokes Raman event additionally samples both the pump and the shifted emission frequency. Molecular orientation, adsorption and collection polarization determine how these fields contribute to the measured response [5–7,12–14]. These effects must be retained together when interpreting a supported surface. The present study converts these requirements into explicit analytical tests. We derive the optimum resonance center for a two-frequency Lorentzian kernel, identify the occupancy threshold for a ranking reversal, and construct a spatial reassignment test that preserves both marginal enhancement distributions. A further bound establishes what can and cannot be inferred when only local products are reported. The underlying reciprocity relation and covariance identity are established results; the contribution is their combined use in quantitative ranking and information-sufficiency tests. Full-wave wavelength scans and one-factor interface sweeps then test these criteria in the prescribed supported-particle system. The motivating architecture is a gold nanoparticle deposit on oxide-covered aluminum, consistent with published particle-on-mirror and gold-on-foil studies [15–18]. Analytical demonstrations are complemented by newly executed, explicitly prescribed full-wave monomer/pair and air/support controls. The numerical benchmark uses ideal planar layers and monodisperses spheres; it is not a reconstruction of a measured deposit. No experimental spectra or sample-specific detection limits are reported.

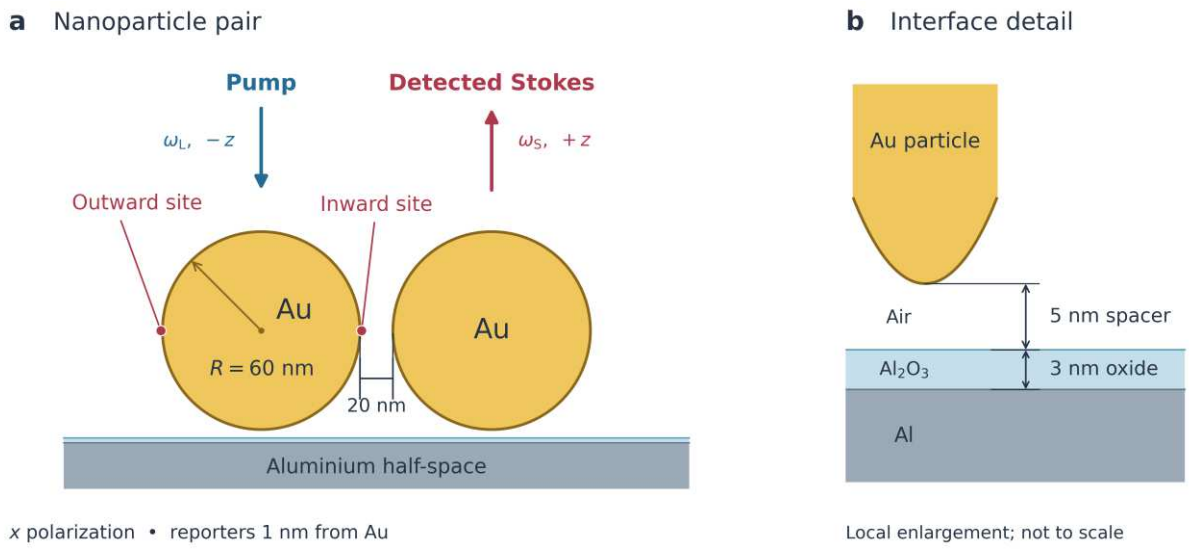


Fig. 1 Prescribed nanoparticle–oxide–aluminum geometry. (a) Gold spheres have radius R = 60 nm and a 20 nm surface gap. Red markers identify inward and outward reporters 1 nm outside the left sphere, at (−9,0,68) and (−131,0,68) nm. Arrows indicate propagation of the x-polarized pump (−z) and detected Stokes mode (+z) for the coupled system. (b) Enlarged interface showing the minimum 5 nm air spacer, 3 nm oxide and aluminum half-space. The local enlargement is not on the scale. This is a geometry schematic, not a field map; reciprocal Stokes illumination propagates along −z

2 Response framework and calculation methods

2.1 Molecular response and normalization

For weak, spontaneous Raman scattering in a linear, reciprocal optical environment, the normalized Raman amplitude for collection mode j is the bilinear contraction

$$A_j(r, O) = f_{rec,j}(r, \omega_s) \cdot \hat{\alpha}^R(O) \cdot f_{exc}(r, \omega^L) \quad (1)$$

The local excitation and reciprocal fields are normalized to a common incident electric-field amplitude. The reciprocal field is obtained by illuminating the structure from the detected optical mode. The normalized Raman tensor $\hat{\alpha}^R$ carries molecular orientation O and any molecular resonance. The bilinear contraction is taken before its squared modulus; complex conjugation is supplied by that modulus, rather than inserted arbitrarily in the reciprocity amplitude [5,19]. A scalar $|E|^4$ estimate is recovered only under additional assumptions about frequency separation, tensor projection and collected modes.

$$Q = p \int q(r, O)\, \Sigma_j w_j |A_j(r, O)|^2 \, d\mu\,; \quad \mathcal{E} = Q/Q_0 \quad (2)$$

Here p is the fraction of supplied molecules occupying accessible sites, q is their normalized conditional distribution, and w_j are consistently normalized collection-mode weights. The reference Q_0 uses the same molecular tensor, illumination and detection convention in a stated homogeneous environment. For a continuous numerical aperture, the mode sum becomes the corresponding angular integral. Equal incident field amplitudes and equal irradiances are interchangeable only for comparisons in the same incident medium. Optical comparisons hold molecular number, incident irradiance and instrumental throughput fixed.

For an x-directed rank-one Raman tensor and a single x-polarized reciprocal mode, define $G^L = |f_{exc,x}|^2$ and $G_s = |f_{rec,x}|^2$. Their product $K = G^L G_s$ is a dimensionless local kernel, not a calibrated signal or a substrate-average enhancement factor. For any fixed molecular sampling distribution,

$$\langle K \rangle q = \langle G^L \rangle q \, \langle G_s \rangle q + Covq(G^L, G_s) \quad (3)$$

Spatial registration is therefore necessary: separate field averages cannot reconstruct the mean kernel unless the covariance is also supplied. A general tensor requires the full amplitude in Eq. (1), including orientation-dependent cross terms.

2.2 Far-field observables and the supported surface

For an isolated finite object in a homogeneous medium, extinction is the sum of absorption and scattering cross-sections. It is determined by interference in the forward direction and the complete electromagnetic solution, rather than by a direct surface average of local intensity. On an opaque support, experimentally relevant observables include specular and diffuse reflectance and particle-induced changes relative to bare foil. A suspension extinction spectrum supported reflectance, and a molecular kernel are distinct observables with distinct reference conventions.

Neither a measured extinction peak height nor its linewidth can be substituted directly for the height and linewidth of a local-field transfer function. Far-field spectra constrain a model; they do not uniquely determine the field at an occupied molecular site. Sections 3 and 4 consequently use prescribed local responses to demonstrate ranking and sampling effects, without claiming that these functions are fitted extinction spectra.

2.3 Reproducible analytical calculations

Optical wavenumber is $s = \omega/(2\pi c)$, expressed in cm^{-1}; wavelengths are vacuum wavelengths in nm. The numerical examples use $\tilde{\nu} = 1580\ cm^{-1}$. The accompanying archive contains analytical implementation, independent bounded optimization, dense-grid checks, material tables, full-wave source and registered complex fields. Analytical maxima agreed with independent numerical optimization to relative differences below 10^{-12}. Online Resource 1 gives full-wave geometry, numerical refinements and field-derived averages separately from the audit of earlier rounded values.

Use of artificial intelligence. OpenAI ChatGPT was used to assist with computational-code development, analytical checking, figure preparation and language editing. Numerical outputs are supported by the retained solver inputs, complex fields and verification records. The authors are responsible for reviewing the methods, computational outputs and final manuscript.

$$s_s = s^L - \tilde{\nu}; \quad \lambda_s = 10^7/(10^7/\lambda^L - \tilde{\nu}) \quad (4)$$

Table 1. Calculated Stokes wavelengths. The denominator in Eq. (4) must remain positive.

Pump λ^L (nm)	Stokes λ_s (nm)	Shift (cm^{-1})
532	580.82	1580
633	703.34	1580
785	896.15	1580

3 Spectral overlap and ranking reversal

3.1 Exact optimum of a two-frequency Lorentzian kernel

Assume identical projected local-intensity transfer functions at excitation and reciprocal emission, each with peak H, half-width at half-maximum h and center s_c. This is a reduced analytical model. It isolates spectral overlap without representing all modes or the material dispersion of a supported deposit.

$$G(s) = H/[1 + ((s - s_c)/h)^2]; \quad K = G(s^L)G(s_s) \quad (5)$$

Let $s_m = (s^L + s_s)/2$, $a = \tilde{\nu}/(2h)$, and $u = (s_c - s_m)/h$. The normalized denominator becomes

$$D(u) = [1 + (u - a)^2][1 + (u + a)^2] = u^4 + 2(1 - a^2)u^2 + (1 + a^2)^2 \quad (6)$$

$$dD/du = 4u(u^2 + 1 - a^2) \quad (7)$$

When $a \leq 1$, the optimum is $u = 0$ and the resonance lies at the pump–Stokes midpoint. When $a > 1$, that point becomes a minimum of K, and two symmetric maxima occur at $u = \pm\sqrt{(a^2 - 1)}$. The optimized kernel is therefore

$$K_{max} = H^2F(a); \quad F(a) = (1 + a^2)^{-2} \; for \; a \leq 1; \quad F(a) = (4a^2)^{-1} \; for \; a > 1 \quad (8)$$

The transition occurs at $h = \tilde{\nu}/2 = 790$ cm⁻¹. Thus, placing a resonance midway between pump and Stokes is optimal only when its width is sufficient. A general rule recommending midpoint tuning for arbitrarily narrow resonances would be incorrect. Wavelength plots also require care: the midpoint is defined in frequency or optical wavenumber, not by the arithmetic mean of wavelengths.

3.2 Quantitative ranking and accessibility threshold

Candidate A has H = 100 and h = 200 cm⁻¹, initially centered at the pump. Candidate B has H = 60 and h = 800 cm⁻¹, centered at the pump–Stokes midpoint. The calculated products are 157.704 and 922.783, respectively, so B gives a 5.851-fold larger kernel despite its lower peak. A laser-only approximation $G(s^L)^2$ gives 10000 for A and approximately 922.783 for B, reversing this ranking. This is a counterexample to single-frequency local-response ranking; an extinction-based ranking has the additional unresolved far-field-to-local mapping.

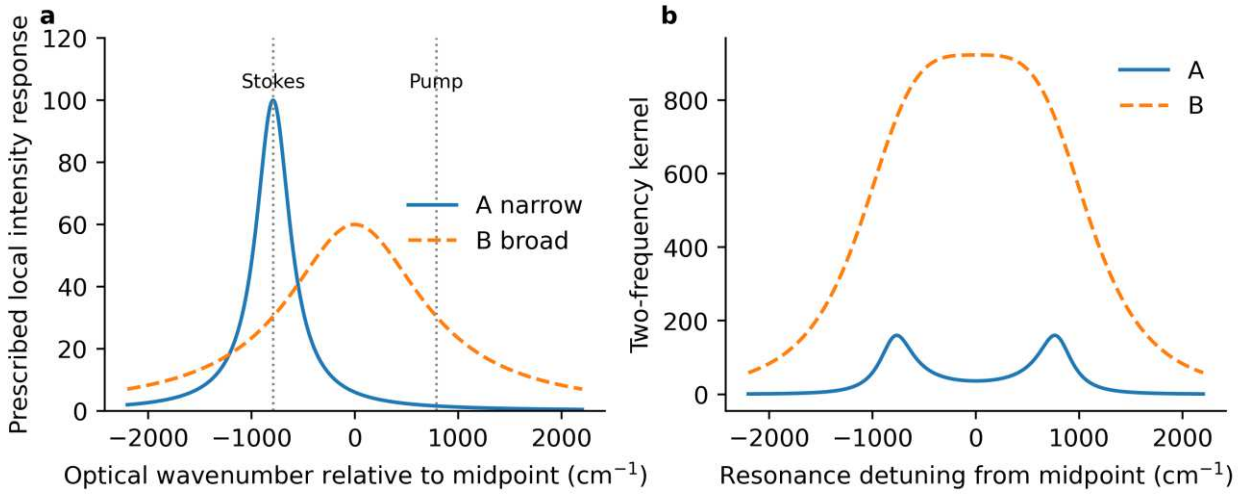


Fig. 2 Prescribed Lorentzian local responses. (a) Intensities at the pump and Stokes frequencies. A shows Stokes-centered; pump centering gives the same product. (b) Kernel versus resonance-center detuning. A has two off-center optima; B has one midpoint optimum. These are analytical curves, not measured extinction spectra

Table 2. Spectral calculations for $\tilde{\nu}$ = 1580 cm⁻¹. K is dimensionless; h is intensity half-width.

Candidate	H	h (cm⁻¹)	Initial K	Optimized K
A	100	200	157.704	160.231
B	60	800	922.783	922.783

Independent center optimization increases A only to 160.231, whereas B remains at 922.783. Their ratio is 5.759. Let M represent an independently specified tensor-projection factor and p an occupancy factor. Under the explicitly separable reduced model, B remains preferred when

$$(p^B M^B)/(p^A M^A) > (H^A)^2 F(a^A)/[(H^B)^2 F(a^B)] = 0.173639 \quad (9)$$

The threshold quantifies a conditional tolerance to reduced sampling of B. It does not estimate adsorption on gold or aluminum oxide. If occupancy and orientation depend on position, they belong inside Eq. (2) and cannot be extracted as independent scalars. Fig. 3 shows the bandwidth dependence and the narrow-to-broad transition. Increasing h at fixed H improves overlap in this mathematical model, but real damping changes H, radiative coupling and spectral weight simultaneously. The result therefore does not recommend increasing material loss.

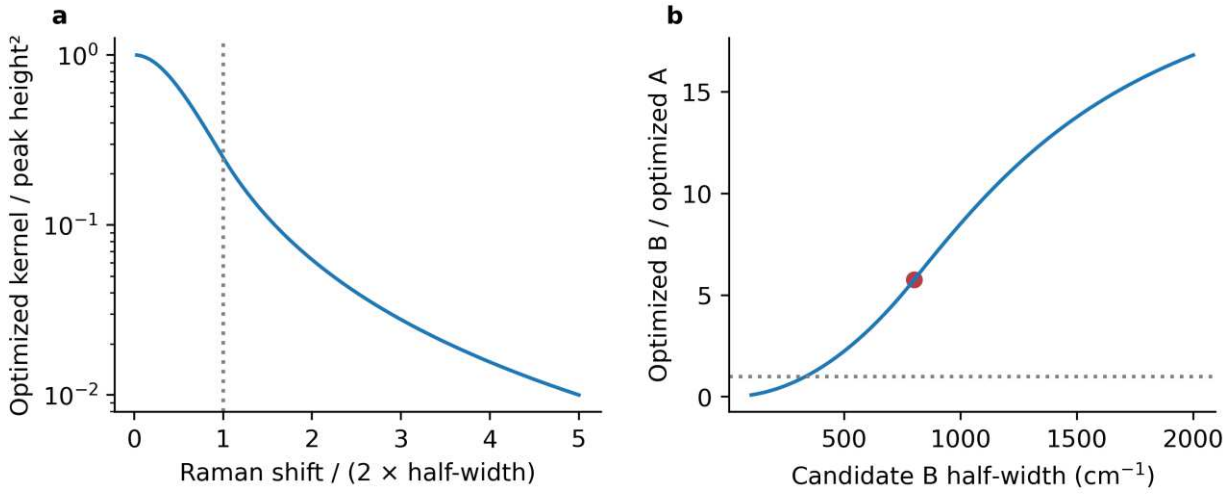


Fig. 3 Analytical bandwidth dependence. (a) Optimized kernel divided by H^2 as a function of $a = \tilde{\nu}/(2h)$; the dotted line marks the change in optimum. (b) Optimized response ratio as candidate B half-width varies at fixed $H^B = 60$, compared with candidate A at $H^A = 100$ and $h^A = 200$ cm^{-1}. The marker denotes $h^B = 800$ cm^{-1}. Holding height fixed is a model assumption, not a materials-design constraint

4 Spatial registration and information sufficiency

4.1 An exact two-site reassignment test

Consider two equally occupied accessible sites with excitation enhancements (1000, 10). Assign reciprocal enhancements (400, 40) in an aligned arrangement and (40, 400) in a reversed arrangement. The marginal distributions, their averages and the product of separate averages are identical. Only the spatial assignment changes. The mean kernels nevertheless differ by a factor of 9.10, as shown in Fig. 4 and Table 3.

$$K = w\, G_1^L G_{S,1} + (1 - w) G_2^L G_{S,2} \quad (10)$$

$$K - K_{sep} = w(1 - w)(G_1^L - G_2^L)(G_{S,1} - G_{S,2}) \quad (11)$$

Here $K_{sep} = [wG^L{}_{,1} + (1 - w)G^L{}_{,2}][wG_{s,1} + (1 - w)G_{s,2}]$. Equation (11) follows by direct expansion and makes the covariance sign explicit. The error vanishes when only one site is occupied or when either enhancement is spatially uniform. At equal occupancy, the separate means estimate underestimates the aligned result by 44.5% but overestimates the reversed result by 405%. No far-field model is assigned to these two constructed arrays, so the example does not claim that a physical structural change preserves an extinction spectrum.

Table 3. Constructed two-site responses at w = 0.5. The two marginal distributions are preserved exactly. These are analytical arrays, not simulated field values.

Arrangement	Mean G^L	Mean G_s	$\bar{K}$	K_{sep}
Aligned	505	220	200200	111100
Reversed	505	220	22000	111100

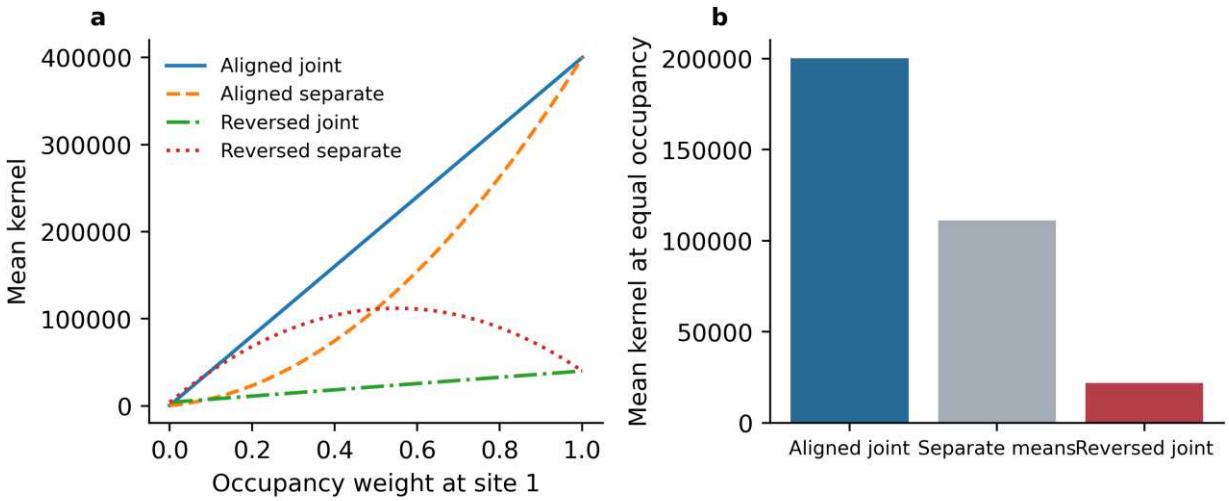


Fig. 4 Spatial reassignment and occupancy. (a) Mean products and products of separate means for the aligned and reversed assignments as occupancy weight w varies. (b) Equal-occupancy comparison. Identical marginal enhancement distributions are compatible with substantially different joint responses. The site values are prescribed analytical inputs; these curves are not maps of an aluminum-supported deposit

4.2 What local products alone can establish

Suppose only $K_1 = G^{L,1}G_{s,1}$ and $K_2 = G^{L,2}G_{s,2}$ are retained. Their equal-weight mean is known, but K_{sep} generally is not. For strictly positive excitation intensities let $r = G^{L,1}/G^{L,2}$. Then

$$K_{sep} = (K_1 + K_2 + rK_2 + K_1/r)/4 \quad (12)$$

The arithmetic–geometric mean inequality gives $rK_2 + K_1/r \geq 2\sqrt{(K_1K_2)}$, hence

$$K_{sep} \geq (\sqrt{K_1} + \sqrt{K_2})^2/4 \quad (13)$$

$$1 - K_{sep}/K \leq 1/2 - \sqrt{(K_1K_2)}/(K_1 + K_2) \quad (14)$$

Equality requires $r = \sqrt{(K_1/K_2)}$, equivalently equal pump-to-Stokes enhancement ratios at the two sites. Without constraints on that ratio, there is no finite upper bound on K_{sep} for positive K_1 and K_2. Thus, the local products determine a maximum possible relative underestimate, not the actual underestimate. This matters when publishing field tables: reporting K alone is insufficient to substantiate a covariance correction. Separate complex field components, or at minimum both projected intensities at registered sites, must also be available. Zero-response cases require taking the corresponding nonnegative limits.

5 Applying the tests to a nanoparticle oxide aluminum interface

5.1 Prescribed geometry and matched controls

Figure 1 specifies the full-wave benchmark geometry. Two gold spheres of radius 60 nm are aligned along x with a 20 nm surface gap. Aluminum occupies $z < 0$; a prescribed 3 nm oxide occupies $0 < z < 3$ nm; a 5 nm air spacer separates each sphere from the oxide. Sphere centers are therefore at $z = 68$ nm and $x = \pm 70$ nm. These values are assumptions, not microscopy measurements or ligand identification. The diameter is 120 nm; confusing radius and diameter would change the electromagnetic problem substantially.

The four controls are a monomer and a pair in air, and a monomer and a pair above the identical oxide/aluminum stack. Each control retains the same site coordinates relative to the left sphere, incident-field normalization, Raman tensor and detection mode. Gold and aluminum optical constants can be specified from Johnson–Christy and Rakić datasets [21–23]; their exact tabulations and interpolation must accompany any numerical implementation. A constant oxide refractive index of 1.65 may be used as an explicit idealization but does not replace a measured oxide dielectric function.

5.2 Coupled boundary problem and separability diagnostic

A layered-medium multiple-scattering formulation [20] writes the outgoing multipole coefficients of particle i as

$$b_i = T_i[a_i^{bg} + \Sigma_{j\neq i} W_{ij}^0 b_j + \Sigma_j W_{ij}^R b_j] \quad (15)$$

T_i is the particle scattering matrix; a_i^{bg} includes the incident field and reflection from the bare stack. W^0 describes direct interparticle propagation and W^R describes support-mediated propagation, including the i = j self-interaction. The oxide and spacer enter the layered response. The system must be solved at the pump and each Stokes frequency before evaluating the molecular tensor contraction. Reducing this problem to independent mirror and pairing multipliers omits feedback between the two coupling pathways.

$$\Xi(r) = K_{supported,pair}(r)\, K_{air,mono}(r)/[K_{air,pair}(r)\, K_{supported,mono}(r)] \quad (16)$$

The null hypothesis of multiplicative separability is Ξ = 1. A departure may represent enhancement or suppression and depends on site, wavelength, tensor and collection mode; it is not a universal support factor or a new microscopic interaction. All denominators must be nonzero, and all four kernels must share a common reference. A statistical interaction contrast can equivalently be expressed as ln Ξ, which changes sign between super multiplicative and sub multiplicative response. The executed benchmark yields inward-site Ξ = 1.6316 at 633 nm and 1.9461 at 785 nm, with outward-site ratios 1.0551 and 1.0400. Thus, the departure from multiplicative separability depends on both frequency and molecular site. These values are reconstructed from the retained complex fields; they are not fitted to the earlier rounded table. A classical dipolar image interaction scales algebraically in its quasistatic limit; no universal exponential coupling law or guaranteed linewidth narrowing is assumed [15,19].

5.3 Numerical verification and benchmark results

For the fixed-geometry benchmark of Table 4, 2πR/λ is approximately 0.596 at 633 nm and 0.480 at 785 nm. The spherical multipole calculation retains $m_{max} = l_{max}$. The selected benchmark run is contour_L18_N40_d0.02_P96, with $l_{max} = m_{max} = 18$, effective-index truncation 40, contour step 0.02, imaginary depth 0.1 and 96 field azimuthal intervals; all registered intensities and kernels are compared under refinement in the Online Resource 1. The final smooth-contour multipole refinement and independent contour-deformation/quadrature comparison each change all registered projected intensities and kernels by less than 0.5% over the four controls, two sites and both frequency pairs. This is numerical self-convergence under the tested refinements, not proof of exactness or experimental validation. The source, input conventions and complex fields permit reconstruction of each table entry.

Material n and k are interpolated linearly in vacuum wavelength from the retained Johnson–Christy gold and Rakić Lorentz–Drude aluminum tables. The oxide is prescribed as nonabsorbing n = 1.65. The same stack and normalization are used at both frequencies and for all matched controls. SMUTHI 2.2.4 supplies the spherical T matrices and layered propagation [20]. A diagonal similarity rescaling b = S y, $S_{ii} = \sqrt{|T_{ii}|}$, improves the numerical scaling of the assembled linear system without changing the Maxwell model; unscaled high-order results were not selected.

For the supported pair, the equal occupancy mean kernel is 2.09×10^5 at 633 nm and 2.185×10^4 at 785 nm. Products of the separately averaged enhancements are 1.293×10^5 and 1.408×10^4, respectively. The directly calculated underestimates of 38.11% and 35.58% follow from registered pump and Stokes fields, rather than from a factorization of the local products. These are means over two prescribed sites, not area-averaged substrate enhancement factors (Table 4 and Fig. 5).

Table 4. Field-derived supported-pair statistics for the idealized benchmark. All values are dimensionless except the pump wavelength. Full individual-field tables and refinement settings are supplied in Online Resource 1.

Pump (nm)	Ξ inward	Mean kernel	Separate means	Underestimate (%)
633	1.6316	2.0898e+05	1.2934e+05	38.110
785	1.9461	21850	14077	35.577

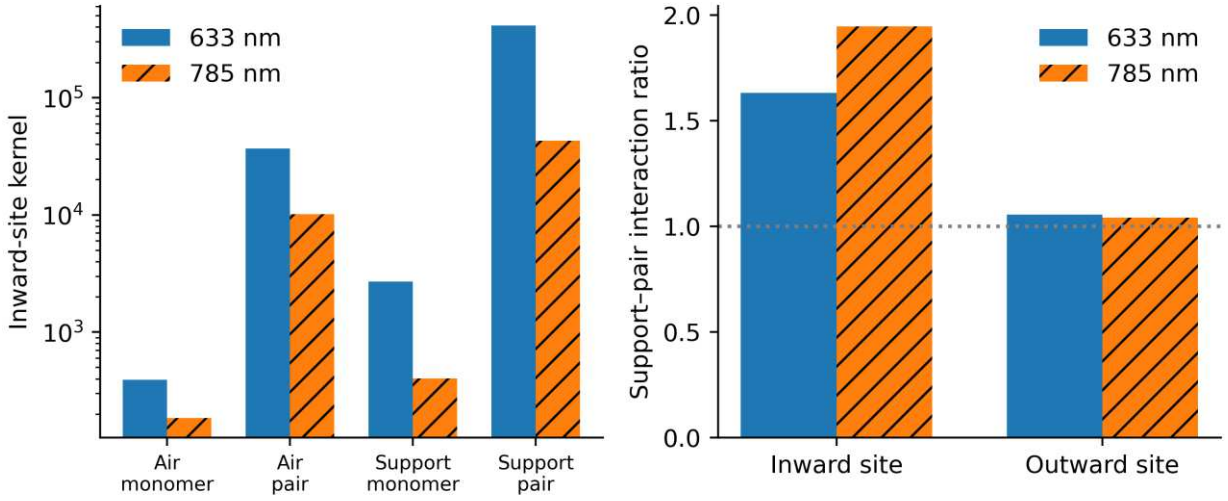


Fig. 5 Full-wave response of the prescribed supported system. Left: inward-site kernels for the four matched controls. Right: support–pair interaction ratios at inward and outward reporter sites. Unity denotes multiplicative separability. The idealized geometry, single-mode detection convention and selected numerical refinement are specified in the text and Supplementary Material

5.4 Wavelength dependence of the supported response

The supported pair was scanned over pump wavelengths of 500–900 nm on a 25 nm grid, with 633 and 785 nm included explicitly. At every pump wavelength, the reciprocal field was solved independently at the Stokes wavelength for $\tilde{\nu} = 1580$ cm^{-1}. The Raman objective is the equally weighted mean $\bar{K} = \tfrac{1}{2}\Sigma_i G^L{}_{,i} G_{s,i}$ at the two prescribed reporter sites. A pump-only proxy, $\tfrac{1}{2}\Sigma_i G^L{}_{,i}{}^2$, uses the same sites and weights. The baseline upward particle-scattering cross-section was also calculated over the air hemisphere, excluding the bare-foil reflected plane wave. It is a scattered-radiation observable, not transmission extinction or total supported-sample reflectance.

The nominal mean kernels at 633 and 785 nm agree with the independently retained fixed-geometry benchmark in Table 4 to 0.133% and 0.025%, respectively. These small differences reflect the independently tested numerical settings; the geometry, reporter definitions and normalization are unchanged.

All three baseline spectral objectives were refined at 5 nm intervals around their coarse-grid maxima. The Raman maximum was similarly refined for the lower and upper endpoints of each geometry sweep. Peak wavelengths below denote the highest sampled response within the stated window; they are not continuous global optima. The expanded calculations use the same material tables and normalization as the fixed-geometry benchmark, with a primary multipole cutoff of 20, effective-index truncation 50, contour step 0.02, imaginary contour depth 0.1 and 96 azimuthal intervals. Reflected fields were evaluated in double precision. Higher order and quadrature checks are documented in Online Resource 1.

For the nominal 3 nm oxide, 5 nm spacer and 20 nm interparticle gap, the sampled Raman-kernel maximum occurs at 595 nm, compared with 580 nm for upward scattering and 680 nm for the pump-only proxy (Fig. 6a). The maximum mean kernel is 2.786×10^5. Selecting the pump-only maximum gives 55.4% of the highest sampled Raman kernel; selecting the upward-scattering maximum gives 88.4%. The separation of these maxima is obtained from the same coupled structure and registered reporter sites. It therefore provides a numerical example of why neither a far-field radiation peak nor a single-frequency fourth-power proxy uniquely selects the maximum two-frequency response. The wavelength-dependent separate-means error is shown in Fig. 6b; its value is not a universal correction factor.

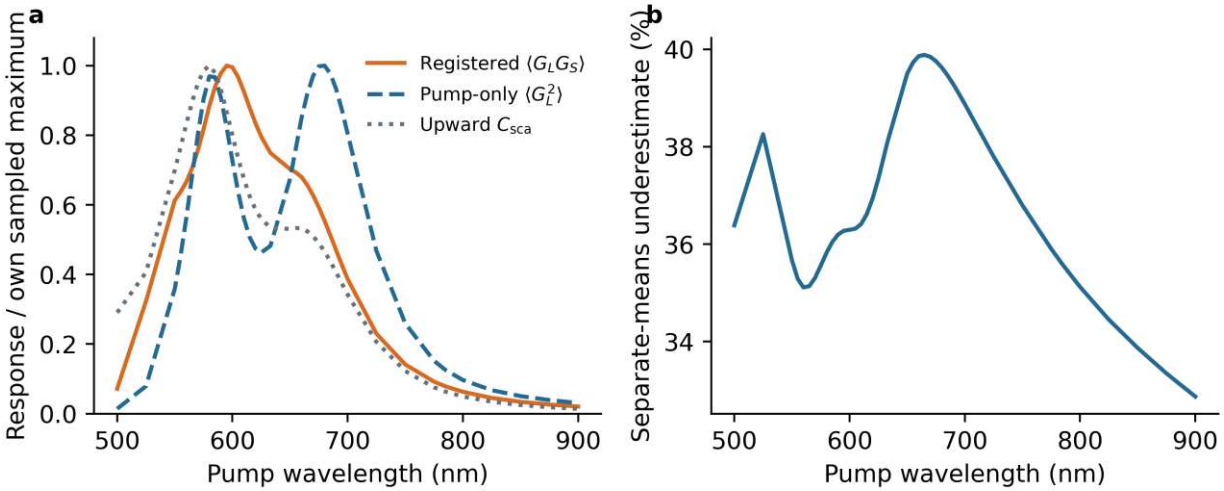


Fig. 6 Calculated baseline spectral response for the prescribed supported pair. (a) The registered mean Raman kernel, pump-only fourth-power proxy and upward particle-scattering cross-section are each normalized to their own sampled maximum. Their units and physical meanings differ. (b) Relative underestimate incurred by multiplying separate site averages. Both panels use equal reporter weights and $\tilde{\nu}$ = 1580 cm^{-1}. Lines connect calculated points, with 5 nm refinement near the sampled maxima. Upward scattering excludes the bare-foil reflected plane wave; it is not extinction or total reflectance

5.5 Sensitivity to oxide spacer and interparticle gap

A one-factor-at-a-time design varies oxide thickness t over 1, 2, 3, 4 and 5 nm; minimum air-spacer thickness s over 3, 4, 5, 6 and 7 nm; and interparticle gap g over 10, 15, 20, 25 and 30 nm. Other dimensions retain the nominal values t = 3 nm, s = 5 nm and g = 20 nm. All five levels were evaluated at 633 and 785 nm; the baseline and the lower and upper endpoints of each sweep were also scanned spectrally. The sphere radius remains 60 nm. Sphere centers are $x = \pm(60 + g/2)$ nm and $z = 60 + t + s$ nm, so varying oxide or spacer thickness changes the height consistently with the specified separation. Reporter sites remain 1 nm outside the left sphere at its inward and outward equators, with unchanged tensor orientation and equal weights.

For each geometric dimension $d \in \{t, s, g\}$, the normalized finite-difference sensitivity at the nominal geometry is

$$S(d;\,\lambda^{L}) \;=\; [d_0/K(d_0)]\,[K(d_0 + \Delta d) - K(d_0 - \Delta d)]/(2\Delta d) \quad (17)$$

The increments are Δt = Δs = 1 nm and Δg = 5 nm. This is a local finite-step diagnostic; the full sampled maximum/minimum ratio quantifies the broader variation over each tested range. Because the wavelength and site distribution are fixed for each comparison, the sensitivity includes both spectral detuning and redistribution of the fields at the occupied sites. It does not isolate adsorption changes or represent a measured manufacturing tolerance.

Table 5. Sensitivities of equal occupancy mean kernel. S(d) is the normalized central finite difference in Eq. (17). Span is the largest divided by the smallest calculated kernel over the five tested parameter values; it is not an uncertainty interval.

Parameter	Tested range	S(d) at 633 nm	S(d) at 785 nm	Span at 633 nm	Span at 785 nm
Oxide thickness	1–5 nm	0.192	0.131	1.29	1.19
Air spacer	3–7 nm	0.856	-0.061	1.95	1.07
Interparticle gap	10–30 nm	-4.909	-5.063	54.41	63.88

The largest sampled response span at 633 nm is associated with interparticle gap (54.41-fold); at 785 nm it is associated with interparticle gap (63.88-fold). Fig. 7 reports the complete five-level comparisons, including any non-monotonic behavior. The sampled Raman maximum shifts from 670 nm at a 10 nm interparticle gap to 585 nm at a 30 nm gap, with t = 3 nm and s = 5 nm held fixed. The endpoint spectra and geometry-dependent sampled maxima are provided in Online Resource 1. These results apply to the specified accessible reporters. A change that increases field confinement in a buried junction need not increase the response at these equatorial sites.

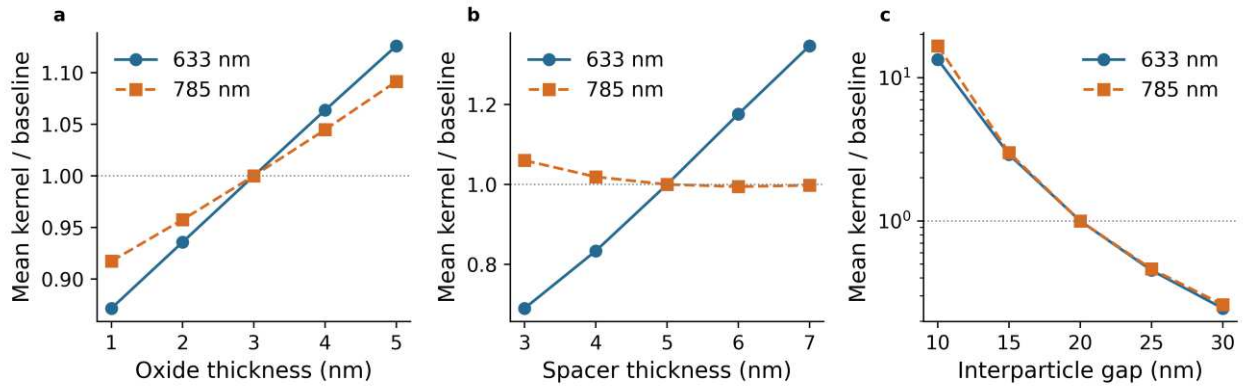


Fig. 7 One-factor sensitivity of the supported-pair mean kernel at 633 and 785 nm. Each curve is normalized to its own wavelength-specific nominal geometry, t = 3 nm, s = 5 nm and g = 20 nm. (a) Oxide thickness. (b) Minimum air spacer. (c) Interparticle gap. Each panel varies only its named parameter; the two reporter sites follow the left particle and retain equal weights. The gap panel uses a logarithmic vertical axis; the oxide and spacer panels are linear. The plotted ratios are not detection limits. The dotted line denotes the nominal response

The one-factor design quantifies conditional sensitivities and spectral shifts but does not estimate interactions between simultaneously varying parameters or establish a globally optimal three-dimensional geometry. The wavelength objective remains a normalized electromagnetic kernel. Molecular dispersion, instrumental throughput and the Stokes-frequency photon factor in Eq. (18) can change the excitation wavelength that maximizes measured counts.

6 Experimental interpretation and limitations

A specific deposit requires microscopy-derived particle dimensions, shapes, gaps, aggregate statistics and areal coverage. Oxide and residue layers require independent surface characterization; foil roughness and drying heterogeneity require spatial sampling. Molecular access to a buried junction cannot be inferred from the local field there. Adsorption, orientation and optical intensity may be correlated and should then enter a joint sampling distribution rather than independent factors.

For opaque foil, total reflectance and specular reflectance must be distinguished. If transmission is negligible and all reflected power is measured, absorptance is $1 - R_{total}$. A decrease in specular reflectance alone can instead arise from diffuse redistribution. Comparisons should include bare foil and a weakly reflecting reference support under matched loading and acquisition conditions, while recognizing that changing support can also change deposition morphology and adsorption [17,18].

Laser selection also depends on the detected objective. At fixed incident irradiance and approximately frequency-independent nonresonant molecular polarizability, Raman power contains an ω_s^4 factor, whereas photon counts contain ω_s^3. A count-rate objective may be written schematically as

$$C(\lambda^L) \propto N_{supplied}\, p\, \eta(\omega_s)\, \omega_s^3 \int q\, \Sigma_j\, w_j |A_j|^2\, d\mu \quad (18)$$

Here η represents wavelength-dependent transmission and detector efficiency, excluding collection factors already included through reciprocal modes. A calculation of normalized K alone cannot establish an optimum photon count, a concentration detection limit or single-molecule sensitivity. Those claims require molecular cross-sections, adsorption and calibration data, background and a stated noise model [5,12].

The analysis assumes linear reciprocal optics, weak spontaneous Raman scattering and a fixed molecular response. It omits chemical enhancement, heating-induced changes, saturation and photochemistry. Nonlocal response and tunnelling require appropriate metal separation and electronic boundary conditions [24–28]. A reporter 1 nm from gold does not by itself establish tunnelling. The prescribed 20 nm interparticle gap is treated classically; the present analytical calculations demonstrate no quantum enhancement or quantum-limited detection threshold.

7 Conclusions

The molecular Raman response at a supported nanoparticle surface depends on registered excitation and reciprocal fields at two frequencies, weighted by molecular access and orientation. A single spectral peak or two separate field averages do not contain that joint information. For prescribed Lorentzian local responses, a lower-peak candidate gives a 5.85-fold larger two-frequency kernel, with a 5.76-fold advantage after independent center optimization. The optimum center changes from a midpoint to two off-center solutions when the Raman shift exceeds twice the intensity half-width.

Spatial reassignment of identical marginal enhancement distributions changes an equal occupancy mean kernel by a factor of 9.10 in the constructed example. The product-only bound shows why kernels alone cannot establish a separate-means error. In the new gold–oxide–aluminum benchmark, registered fields give inward interaction ratios 1.632 and 1.946, and separate-means underestimates of 38.11% and 35.58%. These conditional predictions concern the prescribed geometry and sampled sites. Predicting an experimental deposit additionally requires measured morphology, oxide and spacer properties and molecular distributions.

The spectral scan separates the nominal sampled Raman-kernel maximum at 595 nm from the upward-scattering maximum at 580 nm and the pump-only proxy maximum at 680 nm. Geometry sweeps show that the strength and wavelength dependence of the response depend on oxide, spacer and interparticle separation. These conditional results support joint electromagnetic and molecular-sampling evaluation rather than a universal optical-peak or gap-size rule.

Supplementary information

Analytical details and supplementary numerical results are provided in Online Resource 1 (ESM_1.pdf). The underlying code, fields and computational verification records are supplied in Online Resource 2 (ESM_2.pdf).

References

[1] Kelly KL, Coronado E, Zhao LL, Schatz GC (2003) The optical properties of metal nanoparticles: the influence of size, shape, and dielectric environment. J. Phys. Chem. B 107:668–677. https://doi.org/10.1021/jp026731y

[2] Hutter E, Fendler JH (2004) Exploitation of localized surface plasmon resonance. Adv. Mater. 16:1685–1706. https://doi.org/10.1002/adma.200400271

[3] Anker JN, Hall WP, Lyandres O, Shah NC, Zhao J, Van Duyne RP (2008) Biosensing with plasmonic nanosensors. Nat. Mater. 7:442–453. https://doi.org/10.1038/nmat2162

[4] Moskovits M (1985) Surface-enhanced spectroscopy. Rev. Mod. Phys. 57:783–826. https://doi.org/10.1103/RevModPhys.57.783

[5] Le Ru EC, Etchegoin PG (2006) Rigorous justification of the $|E|^4$ enhancement factor in surface enhanced Raman spectroscopy. Chem. Phys. Lett. 423:63–66. https://doi.org/10.1016/j.cplett.2006.03.042

[6] Stiles PL, Dieringer JA, Shah NC, Van Duyne RP (2008) Surface-enhanced Raman spectroscopy. Annu. Rev. Anal. Chem. 1:601–626. https://doi.org/10.1146/annurev.anchem.1.031207.112814

[7] Lombardi JR, Birke RL (2009) A unified view of surface-enhanced Raman scattering. Acc. Chem. Res. 42:734–742. https://doi.org/10.1021/ar800249y

[8] Zuloaga J, Nordlander P (2011) On the energy shift between near-field and far-field peak intensities in localized plasmon systems. Nano Lett. 11:1280–1283. https://doi.org/10.1021/nl1043242

[9] Fang Y, Seong NH, Dlott DD (2008) Measurement of the distribution of site enhancements in surface-enhanced Raman scattering. Science 321:388–392. https://doi.org/10.1126/science.1159499

[10] Willets KA (2024) Super-resolution surface-enhanced Raman scattering: perspectives on the past, present, and future. ACS Nano 18:27824–27832. https://doi.org/10.1021/acsnano.4c10655

[11] Lu Z, Ji J, Ye H, Zhang H, Zhang S, Xu H (2024) Quantifying the ultimate limit of plasmonic near-field enhancement. Nat. Commun. 15:8803. https://doi.org/10.1038/s41467-024-53210-8

[12] Zhang H, Yang L, Zhang M, Wei H, Tong L, Xu H, Li Z (2024) A statistical route to robust SERS quantitation beyond the single-molecule level. Nano Lett. 24:11116–11123. https://doi.org/10.1021/acs.nanolett.4c03507

[13] Yao L, Hao Q, Li M, Fan X, Li G, Tang X, Wei Y, Wang J, Qiu T (2023) Flexible plasmonic nanocavities: a universal platform for the identification of molecular orientations. Nanoscale 15:6588–6595. https://doi.org/10.1039/D3NR01059G

[14] Craciun AM, Stoia D, Azziz A, Astilean S, Focsan M, Lamy de la Chapelle M (2025) Investigation of local field enhancement near plain and shell-coated gold nanospheres for the optimization of surface enhanced spectroscopy. RSC Adv. 15:20848–20862. https://doi.org/10.1039/D5RA03633J

[15] Baumberg JJ, Aizpurua J, Mikkelsen MH, Smith DR (2019) Extreme nanophotonics from ultrathin metallic gaps. Nat. Mater. 18:668–678. https://doi.org/10.1038/s41563-019-0290-y

[16] Barik P, Pal S, Pradhan M (2021) On-demand nanoparticle-on-mirror (NPoM) structure for cost-effective surface-enhanced Raman scattering substrates. Spectrochim. Acta A Mol. Biomol. Spectrosc. 263:120193. https://doi.org/10.1016/j.saa.2021.120193

[17] Gudun K, Elemessova Z, Khamkhash L, Ralchenko E, Bukasov R (2017) Commercial gold nanoparticles on untreated aluminum foil: versatile, sensitive, and cost-effective SERS substrate. J. Nanomater. 2017:9182025. https://doi.org/10.1155/2017/9182025

[18] Arbuz A, Sultangaziyev A, Rapikov A, Kunushpayeva Z, Bukasov R (2022) How gap distance between gold nanoparticles in dimers and trimers on metallic and non-metallic SERS substrates can impact signal enhancement. Nanoscale Adv. 4:268–280. https://doi.org/10.1039/D1NA00114K

[19] Novotny L, Hecht B (2012) Principles of nano-optics, 2nd edn. Cambridge University Press, Cambridge. https://doi.org/10.1017/CBO9780511794193

[20] Egel A, Czajkowski KM, Theobald D, Ladutenko K, Kuznetsov AS, Pattelli L (2021) SMUTHI: a Python package for the simulation of light scattering by multiple particles near or between planar interfaces. J. Quant. Spectrosc. Radiat. Transf. 273:107846. https://doi.org/10.1016/j.jqsrt.2021.107846

[21] Johnson PB, Christy RW (1972) Optical constants of the noble metals. Phys. Rev. B 6:4370–4379. https://doi.org/10.1103/PhysRevB.6.4370

[22] Polyanskiy MN (2024) RefractiveIndex.info database of optical constants. Sci. Data 11:94. https://doi.org/10.1038/s41597-023-02898-2

[23] Rakić AD, Djurišić AB, Elazar JM, Majewski ML (1998) Optical properties of metallic films for vertical-cavity optoelectronic devices. Appl. Opt. 37:5271–5283. https://doi.org/10.1364/AO.37.005271

[24] Esteban R, Borisov AG, Nordlander P, Aizpurua J (2012) Bridging quantum and classical plasmonics with a quantum-corrected model. Nat. Commun. 3:825. https://doi.org/10.1038/ncomms1806

[25] Savage KJ, Hawkeye MM, Esteban R, Borisov AG, Aizpurua J, Baumberg JJ (2012) Revealing the quantum regime in tunnelling plasmonics. Nature 491:574–577. https://doi.org/10.1038/nature11653

[26] Mortensen NA, Raza S, Wubs M, Søndergaard T, Bozhevolnyi SI (2014) A generalized non-local optical response theory for plasmonic nanostructures. Nat. Commun. 5:3809. https://doi.org/10.1038/ncomms4809

[27] Zhu W, Esteban R, Borisov AG, Baumberg JJ, Nordlander P, Lezec HJ, Aizpurua J, Crozier KB (2016) Quantum mechanical effects in plasmonic structures with subnanometre gaps. Nat. Commun. 7:11495. https://doi.org/10.1038/ncomms11495

[28] Ciracì C, Hill RT, Mock JJ, Urzhumov Y, Fernández-Domínguez AI, Maier SA, Pendry JB, Chilkoti A, Smith DR (2012) Probing the ultimate limits of plasmonic enhancement. Science 337:1072–1074. https://doi.org/10.1126/science.1224823

Statements and Declarations

Funding

This work received no direct project grant. The authors acknowledge the general institutional support of the Austrian Research Promotion Agency (FFG), the Brazilian National Council for Scientific and Technological Development (CNPq), and the Brazilian Federal Agency for Support and Evaluation of Graduate Education (CAPES).

Competing interests

Patrícia M. A. Farias reports co-ownership of Phornano. Andreas Stingl is affiliated with Phornano Holding GmbH. These relationships are disclosed for editorial assessment. The remaining authors declare that they have no known competing financial interests or personal relationships that could have appeared to influence the work reported in this paper.

Author contributions

Patrícia M. A. Farias: Conceptualization, Methodology, Formal analysis, Validation, Investigation, Resources, Writing – original draft, Writing – review & editing. Priscila Vilemen: Conceptualization, Formal analysis, Writing – review & editing. Nathalia B. Lima: Formal analysis, Writing – review & editing. Andreas Stingl: Conceptualization, Investigation, Methodology, Validation, Formal analysis, Writing – review & editing. Olavo Cardozo: Conceptualization, Methodology, Validation, Formal analysis, Investigation, Writing – review & editing.

Data availability

The data supporting the analytical and numerical results are supplied with this article in Online Resources 1 and 2. Online Resource 2 includes exact tabulated material inputs, simulation grids, registered complex fields, outgoing multipole coefficients, numerical-refinement records, derived tables and verification results. No experimental data are reported. The optical-constant sources are references [21–23].

Code availability

The analytical full-wave implementation retained solver source, dependency specifications and figure-generation scripts are provided in Online Resource 2.

Supplementary Files

This is a list of supplementary files associated with this preprint. Click to download.

- ESM2.pdf
- ESM1.pdf